

XAI-CLIP: ROI-Guided Perturbation Framework for Explainable Medical Image Segmentation in Multimodal Vision-Language Models

Thuraya Alzubaidi¹, Sana Ammar¹, Maryam Alsharqi², Islem Rekik³, Muzammil Behzad^{1,4,*}

¹King Fahd University of Petroleum and Minerals, Saudi Arabia

²Massachusetts Institute of Technology, US

³Imperial College London, UK

⁴KFUPM-SDAIA Joint Research Centre for Artificial Intelligence, Saudi Arabia

Abstract— Medical image segmentation is a critical component of clinical workflows, enabling accurate diagnosis, treatment planning, and disease monitoring. However, despite the superior performance of transformer-based models over convolutional architectures, their limited interpretability remains a major obstacle to clinical trust and deployment. Existing explainable artificial intelligence (XAI) techniques, including gradient-based saliency methods and perturbation-based approaches, are often computationally expensive, require numerous forward passes, and frequently produce noisy or anatomically irrelevant explanations. To address these limitations, we propose XAI-CLIP, an ROI-guided perturbation framework that leverages multimodal vision-language model embeddings to localize clinically meaningful anatomical regions and guide the explanation process. By integrating language-informed region localization with medical image segmentation and applying targeted, region-aware perturbations, the proposed method generates clearer, boundary-aware saliency maps while substantially reducing computational overhead. Experiments conducted on the FLARE22 and CHAOS datasets demonstrate that XAI-CLIP achieves up to a 60% reduction in runtime, a 44.6% improvement in dice score, and a 96.7% increase in Intersection-over-Union for occlusion-based explanations compared to conventional perturbation methods. Qualitative results further confirm cleaner and more anatomically consistent attribution maps with fewer artifacts, highlighting that the incorporation of multimodal vision-language representations into perturbation-based XAI frameworks significantly enhances both interpretability and efficiency, thereby enabling transparent and clinically deployable medical image segmentation systems.

Index Terms— Artificial Intelligence, Computer Vision, Medical Image Segmentation, Explainable AI, Perturbation Methods, Vision-Language Models, Interpretability

I. INTRODUCTION

MEDICAL image segmentation is a fundamental part of clinical workflows, allowing clinicians to assess anatomical boundaries and pathological structures for decision making in critical areas such as oncology, neurology, and cardiology [1]. Recent segmentation models that leverage transformer-based architectures far surpass traditional CNNs

by effectively modeling long-range dependencies and capturing both global and local features, making them particularly effective for medical image segmentation tasks [2]. However, the transparency of their decision-making processes remains ambiguous. A recent study found that about 76% of medical imaging competitions failed to provide labeling instructions, underscoring the lack of clarity in how AI models are trained and validated, particularly for complex modalities like multi-parametric MRI and CT scans [3]. This makes interpretability challenges a significant barrier for clinical adoption. Consequently, there is a need for explainable AI frameworks that can enhance transparency and unlock the black-box nature of these models [4], allowing clinicians to understand and trust AI decisions and deploy such models responsibly.

In this context, the current medical XAI methods face two key challenges. Gradient-based approaches, such as, Grad-CAM, generate saliency maps efficiently but occasionally highlight low-level features misaligned with anatomical structures [5]. On the other hand, perturbation-based methods iteratively modify inputs to quantify feature importance [6], yet their exhaustive image-wide sampling incurs high computational costs as they apply perturbations even to regions outside of anatomically relevant structures, requiring hundreds of forward passes for a single explanation.

To address these gaps, we propose XAI-CLIP, an ROI-guided perturbation framework leveraging contrastive vision-language modeling as shown in Fig 1. By constraining perturbations to anatomically salient regions using the multimodal embeddings, our framework minimizes computational overhead while ensuring clinically meaningful explanations. Specifically, our framework utilizes a multimodal architecture that embeds visual and textual information in a shared representational space. The model enables zero-shot classification by measuring visual-semantic alignment between images and textual descriptions. These features can be used to extract clinically significant relationships, producing more meaningful saliency maps that align with anatomical structures and pathological regions of interest.

The primary segmentation backbone employed in this study is MedSAM (Medical Segment Anything Model) [2], a

* Corresponding author. Email: muzammil.behzad@kfupm.edu.sa

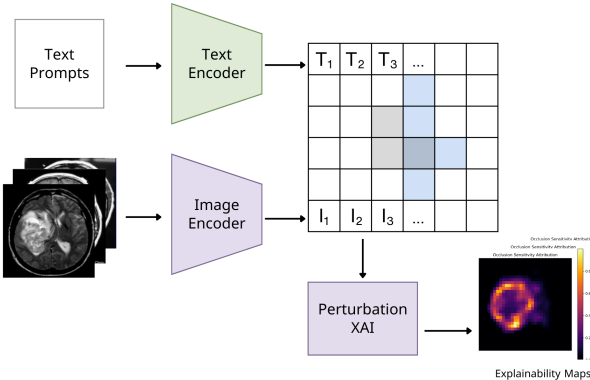


Fig. 1. Overview of the XAI-CLIP framework. Text and image inputs are encoded using vision and text encoders. A joint embedding space guides region-restricted perturbation-based XAI, producing anatomically aligned explainability maps.

transformer-based framework derived from the Segment Anything Model (SAM) [7] and adapted for general-purpose medical image segmentation across multiple imaging modalities, including MRI, CT, and ultrasound. In this work, MedSAM serves as a representative high-performing segmentation model to evaluate the proposed explainability framework rather than as a central contribution of the study. The focus of the investigation remains on assessing the effectiveness and generality of the proposed XAI-CLIP approach in enhancing the interpretability of medical image segmentation outputs. To this end, both qualitative and quantitative analyses are conducted using samples drawn from established benchmark datasets, namely FLARE22 [8] and CHAOS [9], which provide diverse anatomical structures and imaging characteristics suitable for evaluating explanation quality.

The explanatory performance of XAI-CLIP is systematically compared against existing perturbation-based explainability methods to examine its ability to generate anatomically meaningful and visually coherent attribution maps. Rather than emphasizing experimental configurations, the discussion centers on the methodological advantages introduced by region-guided perturbations, which enable more focused and semantically aligned explanations. The proposed framework demonstrates a consistent ability to reduce unnecessary perturbations and suppress redundant activations, leading to clearer saliency maps with improved boundary localization and fewer visual artifacts. We present detailed quantitative evaluations and computational efficiency analyses, conducted under different hardware configurations, later in the paper, where the proposed method is shown to offer substantial runtime improvements over conventional perturbation strategies without compromising explanation fidelity.

II. RELATED WORK

With the emergence of the Segment Anything Model (SAM), a large-scale foundation model for image segmentation that enables prompt-driven and zero-shot generalization [10], [11], significant research attention has been directed toward its adaptation for medical imaging applications [12]. SAM's architecture, composed of a high-capacity image encoder, a flexible prompt encoder, and a lightweight mask

decoder, provides a generalizable framework that can be repurposed across diverse segmentation tasks. Its promptable design has motivated extensive exploration into leveraging foundation models for medical image segmentation, where data scarcity and modality heterogeneity remain persistent challenges.

As an extension of SAM, MedSAM [2], [12] represents a notable adaptation that is tailored to the medical domain through large-scale fine-tuning on approximately 1.57 million image-mask pairs spanning over ten imaging modalities and more than thirty cancer types. This broad training strategy enables MedSAM to generalize across modalities ranging from computed tomography to dermatoscopy without relying on task-specific model variants. Empirical evaluations demonstrate strong segmentation performance across multiple benchmarks, with substantial improvements over conventional convolutional and transformer-based baselines. Nevertheless, the reliance on bounding-box prompts introduces limitations in anatomically complex scenarios, particularly in cases involving branching or overlapping vascular structures, where a single bounding box may inadequately capture fine-grained spatial distinctions.

More recently, SemiSAM+ has been introduced as a semi-supervised medical image segmentation framework that integrates SAM with task-specific segmentation networks [13]. Rather than retraining the frozen SAM encoder, the method exploits SAM-generated priors to guide pseudo-label propagation, followed by refinement using downstream architectures. This strategy demonstrates strong performance in low-annotation regimes, achieving competitive Dice scores with only a small number of labeled samples on benchmark datasets [13]. SemiSAM+ reflects a broader trend toward coupling foundation models with lightweight adaptation mechanisms, aligning with recent approaches that employ adapter-based tuning for clinical deployment [14], [15]. Despite its advantages, the framework remains sensitive to prompt quality, with segmentation accuracy degrading in regions with ambiguous or weak anatomical boundaries. Complementary efforts have also explored knowledge distillation strategies to further enhance semi-supervised segmentation performance [16].

Beyond foundation model adaptations, alternative architectural paradigms have been investigated to improve segmentation efficiency and scalability. Ruan et al. proposed VM-UNet, a segmentation network based entirely on state space models, replacing conventional convolutional and self-attention blocks with Vision State Space modules derived from Mamba [15]. The resulting architecture significantly reduces computational complexity while maintaining competitive accuracy, achieving strong Dice scores across multiple datasets and outperforming transformer-based counterparts such as Swin-UNet. This work highlights the potential of state space models as an efficient alternative to attention-based architectures in medical image segmentation.

In a related direction, Wu et al. introduced Med-SAM, an adapter-based framework that augments a frozen SAM backbone with lightweight bottleneck modules to enable effective medical image segmentation [17]. The proposed Space-Depth Transpose mechanism facilitates the extension of a 2D vision transformer encoder to volumetric data, enabling efficient 3D adaptation with a limited number of trainable

parameters. While Med-SAM achieves strong segmentation accuracy with substantially fewer tunable weights compared to transformer-based baselines, its performance remains sensitive to prompt design, with notable degradation observed under reduced prompt overlap. Complementing these efforts, Ultra-Light VM-UNet further demonstrates the feasibility of highly compact state space-based architectures, achieving competitive performance on skin lesion segmentation tasks with minimal parameter and computational budgets [18]. Together, these studies underscore ongoing efforts to balance segmentation accuracy, computational efficiency, and adaptability in modern medical image segmentation models.

A. Explainable AI in Medical Image Analysis

Explainable artificial intelligence has received increasing attention in medical imaging, driven by the need for transparency and accountability in clinical decision-making. In this regard, Fontes et al. [19] presented a domain-specific taxonomy that systematically categorizes XAI techniques according to imaging modalities and associated clinical tasks. Their review analyzed nine representative studies published between 2021 and 2023, encompassing a range of explainability paradigms, including prototype-based, retrieval-based, counterfactual, and generative adversarial approaches. While the study provides valuable conceptual organization of existing methods, it does not include quantitative performance aggregation and limits its scope to English-language publications within a relatively narrow temporal window.

Addressing limitations in earlier surveys, Hou et al. [20] presented a comprehensive review of self-explainable artificial intelligence (S-XAI) methods for medical image analysis, encompassing more than 200 studies published between 2018 and 2024. The authors structured the literature along three complementary dimensions, input-level, model-level, and output-level explainability, and reported a substantial increase in research activity, with medical imaging accounting for approximately half of all XAI-related publications. In addition, the survey compiled an extensive resource table covering over 70 publicly available datasets. However, while performance metrics were reported across studies, the absence of standardized experimental settings limits direct quantitative comparison.

Building upon these conceptual frameworks, Iglesias et al. [21] proposed MOC-VAE, an explanation method that employs a SPEA2 optimizer to identify minimal perturbations in the latent space that induce misclassification. The proposed approach achieved a high degree of overlap between generated saliency maps and annotated pathological regions, surpassing several competing methods by a notable margin. Nevertheless, the underlying model exhibits relatively modest diagnostic accuracy compared to state-of-the-art chest X-ray classifiers, which constrains its clinical applicability despite improved explainability. From a theoretical standpoint, Abe and Asai [22] introduced a perturbation-based explanation framework that quantifies local input sensitivity via Jacobian matrix analysis. Their method enables instance-specific, data-free explanations that align with key clinical interpretability requirements. While

the framework is mathematically well-founded, the study does not provide quantitative validation on medical imaging benchmarks, leaving its practical effectiveness largely unexplored.

In a collaborative learning context, Mastoi et al. [23] developed an interpretable federated learning pipeline for brain tumor classification, training a GoogLeNet architecture on distributed MRI data while preserving patient privacy. The proposed ten-client framework achieved high classification accuracy across multiple tumor categories. Although Grad-CAM visualizations were incorporated into the inference process, the work did not include a quantitative evaluation of explanation quality or consistency, limiting insight into the reliability of the generated saliency maps.

In domain-specific applications, Yoshida et al. [24] fine-tuned a foundation model for optical coherence tomography (OCT) image classification and employed relevance propagation to generate saliency maps. Their analysis led to the identification of previously unreported imaging biomarkers with high specificity. However, the attribution maps produced by the explanation method were not consistently aligned with pathological regions, suggesting susceptibility to over-attribution and reduced robustness in certain cases.

Despite these advances across surveys, theoretical frameworks, collaborative learning, and specialty applications, many existing XAI approaches in medical imaging continue to operate primarily at the pixel level, without incorporating explicit semantic priors or anatomically meaningful region constraints. This lack of semantic grounding limits the interpretability and clinical relevance of generated explanations, particularly in complex medical imaging scenarios where contextual understanding is essential.

B. Vision-Language Models in Medical Images

Vision-language models (VLMs) have demonstrated significant potential for medical image analysis through joint visual-textual representation learning [25], exemplified by contrastive language-image pretraining (CLIP) [26]. In early foundational work, Poudel et al. [27] systematically evaluated vision-language segmentation models on 2D medical image segmentation tasks across eleven heterogeneous datasets. Their study showed that the model achieved strong segmentation performance, reaching a dice score of 92.40% on the BKAI dataset, while exhibiting substantially improved generalization compared to convolutional baselines, particularly in cross-dataset evaluations. Notably, the model maintained robust performance in out-of-distribution settings, significantly outperforming UNet when transferred between datasets. Despite these encouraging results, the authors observed limited utilization of textual semantics in CLIPSeg-based models, and unexpectedly weaker performance from BiomedCLIP variants, even when pretrained on large-scale medical image-text corpora [27].

To address the computational and parameter inefficiency of earlier VLM-based segmentation approaches, Dhakal et al. [28] introduced VLSM-Adapter, a parameter-efficient fine-tuning strategy based on lightweight adapters. Their approach reduced the number of trainable parameters to approximately

three million while achieving performance comparable to full fine-tuning across multiple medical datasets. In particular, the CLIPSeg Dense Adapter variant demonstrated strong efficiency, outperforming SAN with significantly fewer parameters and remaining competitive with CRIS despite an order-of-magnitude reduction in trainable weights. However, these gains were accompanied by sensitivity to adapter placement, and performance gaps persisted on certain datasets when compared to fully fine-tuned models.

Moving beyond single-model adaptations, Dietlmeier et al. [29] proposed an ensemble-based framework that combines CLIP-based VLMs with lightweight UNet architectures. Their approach integrates feature representations through concatenation and Efficient Channel Attention mechanisms, enabling complementary strengths between multimodal and convolutional components. This ensemble strategy yielded notable improvements in segmentation accuracy across several datasets, particularly for BiomedCLIPSeg-based variants. Nevertheless, the method exhibited modality-dependent variability, with certain datasets showing reduced performance relative to baseline VLM models, highlighting challenges in achieving consistent gains across diverse imaging domains.

Rather than focusing solely on architectural refinements, Chen et al. [30] addressed reasoning deficiencies in VLM-based segmentation by introducing CausalCLIPSeg, which incorporates causal intervention mechanisms for referring medical image segmentation. Their framework improved both dice and mIoU scores over transformer-based baselines by enforcing causal consistency between textual queries and pixel-level predictions. While the cross-modal decoding strategy enhanced text-to-pixel alignment, its reliance on vision-language models pretrained exclusively on natural images constrained its ability to fully capture specialized medical terminology and domain-specific semantics.

To strengthen cross-modal interaction, Sultan et al. [31] proposed BiPVL-Seg, a bidirectional fusion framework augmented with global-local contrastive alignment. This design enabled deeper information exchange between vision and language encoders while aligning representations at both concept and class levels. The resulting model achieved consistent performance improvements across multiple datasets, including higher dice scores and reduced Hausdorff distance. Complementarily, Chen et al. [32] reframed vision-language correspondence as a graph matching problem through BiVLGM, preserving intra-modal structural relationships and yielding substantial gains over strong convolutional and hybrid baselines on histopathology benchmarks.

Recognizing the importance of domain knowledge, Nath et al. [33] introduced VILA-M3, which integrates expert medical knowledge via instruction-based fine-tuning. Their large-scale model achieved strong performance across medical question answering and classification benchmarks, outperforming existing medical VLMs by a significant margin. However, this specialization introduced trade-offs, including degraded performance on general-domain tasks and reliance on external expert systems, which may limit scalability and accessibility in real-world clinical settings.

From a broader perspective, Hartsock and Rasool [34]

provided a comprehensive survey of medical VLMs with a focus on report generation and visual question answering. Their analysis categorized a wide range of models and datasets while emphasizing the growing role of parameter-efficient fine-tuning techniques such as LoRA. Although several models achieved strong performance on radiology-centric benchmarks, the authors identified notable evaluation biases and highlighted underrepresentation of other clinically important domains, including pathology and surgical imaging.

In parallel work related to segmentation, Liang et al. [35] examined vision foundation models for medical applications, with particular attention to efficient adaptations of SAM-based architectures. Their study demonstrated that lightweight variants, enabled through techniques such as low-rank adaptation, could deliver substantial inference speedups without compromising accuracy. Despite these engineering advances, the authors noted that many architectural modifications lack formal performance guarantees, while knowledge distillation methods often suffer from semantic mismatches between natural and medical image domains.

Despite significant progress across architectural design, efficiency optimization, causal reasoning, and domain adaptation, medical VLMs continue to face persistent challenges that hinder clinical adoption. These include modality bias, limited coverage of diverse medical datasets, insufficient integration of spatial and semantic prompts, and high computational demands. Most critically, existing approaches often lack robust mechanisms for interpretable saliency or semantically grounded attribution, underscoring the need for explainability-aware frameworks that balance interpretability, efficiency, and clinical relevance in high-stakes medical decision-making environments.

C. CLIP in Medical Domain

CLIP-based approaches have attracted growing interest in medical imaging due to their capacity for zero-shot transfer and multimodal representation learning. Zhao et al. [36] presented a comprehensive survey of CLIP adaptations for medical imaging, analyzing 224 studies and proposing a three-level taxonomy to categorize methodological trends. Their benchmark analysis demonstrated that domain-specialized CLIP variants, such as BiomedCLIP, achieved near-saturated accuracy across multiple imaging domains, substantially outperforming general-domain medical CLIP models. Despite its breadth, the survey exhibits a strong emphasis on two-dimensional imaging modalities and relies predominantly on a single evaluation metric, limiting insights into robustness and cross-modal generalization.

In applied segmentation settings, Aleem et al. [37] proposed SaLIP, a zero-shot medical image segmentation framework that integrates SAM with CLIP-based region ranking. The method generates candidate masks using SAM, ranks them via vision-language similarity scores computed from automatically generated prompts, and subsequently refines segmentation through re-prompting. SaLIP demonstrated promising performance across several imaging modalities; however, its effectiveness depends critically on the ability of SAM to

generate candidate masks that sufficiently cover the target anatomy. Furthermore, the limited spatial reasoning capacity of CLIP constrains its ability to reliably distinguish anatomically adjacent structures.

To improve robustness and generalization across modalities, Khattak et al. [38] introduced UniMed-CLIP, a dual-encoder vision-language model trained on a large-scale, multimodal medical image-text corpus. By employing a multi-caption supervision strategy, the model achieved notable improvements in zero-shot performance across multiple datasets while requiring substantially less training data than comparable models. Although UniMed-CLIP demonstrates strong cross-dataset generalization, its reliance on caption-level supervision provides limited spatial grounding, which restricts its applicability for fine-grained localization and segmentation tasks.

Focusing on few-shot anomaly detection, Zhang et al. [39] proposed MediCLIP, which adapts CLIP through learnable prompts, vision-side adapters, and synthetic anomaly generation. Their approach significantly improved both image-level and pixel-level anomaly detection performance under limited data regimes and demonstrated cross-dataset generalization without additional fine-tuning. Nonetheless, the use of fixed hyperparameters across heterogeneous modalities and the absence of standardized evaluation protocols limit the generalizability of the reported results.

Integrating vision-language models directly with segmentation pipelines, Koleilat et al. [40] introduced MedCLIP-SAMv2, which combines fine-tuned vision-language representations with SAM-based mask refinement. Their framework leverages saliency-driven prompting to guide segmentation and achieves substantial gains in both retrieval and segmentation performance across multiple modalities. However, the method remains highly sensitive to prompt formulation, with segmentation accuracy varying considerably under minor changes in textual input, underscoring ongoing challenges in achieving stable and reliable vision-language-guided segmentation in medical imaging. A detailed overview of these methods is provided in Table I.

III. THE PROPOSE XAI-CLIP METHOD

A. Preprocessing

Our preprocessing pipeline transforms raw medical images into standardized formats suitable for our proposed pipeline. The process begins with standard input handling, including directory reading and format verification. Images are resized to 224×224 pixels using area interpolation to maintain aspect ratio, followed by grayscale conversion using the BT.601 luminance standard when necessary [47]. One of the core contribution of our pipeline is the adaptive contrast enhancement technique that adjusts processing parameters based on the input image characteristics.

We first separate the foreground from the background using intensity thresholding:

$$\text{Mask}(x, y) = \begin{cases} 1, & \text{if } I(x, y) < T_{\text{bg}} \\ 0, & \text{otherwise} \end{cases}, \quad (1)$$

where $I(x, y)$ is pixel intensity at position (x, y) , and T_{bg} is the background threshold.

We first identify background regions and exclude them from the enhancement process to avoid amplifying noise and non-informative pixels. A binary region-of-interest (ROI) mask is then applied to isolate foreground anatomical structures, enabling targeted and anatomically meaningful preprocessing. We subsequently perform percentile-based contrast stretching, in which the effective intensity range is adaptively determined from the foreground pixel distribution. Specifically, the lower and upper intensity bounds are computed using the 5th and 95th percentile values of the foreground region histogram, providing robust normalization while mitigating the influence of extreme outliers. By restricting enhancement operations to foreground pixels within this adaptive range, we improve structural visibility and ensure consistent contrast enhancement across diverse medical imaging modalities and acquisition conditions as:

$$F = \{ I(x, y) \mid \text{Mask}(x, y) = 0 \}. \quad (2)$$

The lower and upper intensity bounds are then determined using the 5th and 95th percentiles of the foreground distribution:

$$\begin{aligned} p_{\text{low}} &= \text{percentile}(F, 5), \\ p_{\text{high}} &= \text{percentile}(F, 95). \end{aligned} \quad (3)$$

Finally, linear contrast stretching is applied to each pixel as:

$$I_{\text{str}}(x, y) = \begin{cases} 0 & I(x, y) \leq p_{\text{low}} \\ \frac{255 \cdot [I(x, y) - p_{\text{low}}]}{p_{\text{high}} - p_{\text{low}}} & p_{\text{low}} < I(x, y) < p_{\text{high}} \\ 255 & I(x, y) \geq p_{\text{high}} \end{cases}, \quad (4)$$

This approach provides robust normalization across varied imaging conditions without relying on fixed global thresholds. For local contrast enhancement, we employ Contrast Limited Adaptive Histogram Equalization (CLAHE) [48] with an 8×8 tile grid. The histogram clipping mechanism prevents noise amplification in homogeneous regions:

$$\begin{aligned} H'_T(b) &= \min(H_T(b), C) + \frac{1}{256} \sum_{i=1}^{256} \max(0, H_T(i) - C) \\ \text{subject to } C &= \frac{2.0 \cdot N_{\text{pixels}}}{256} \end{aligned} \quad (5)$$

The cumulative distribution function is computed as:

$$\text{CDF}(b) = \sum_{k=1}^b H'_T(k). \quad (6)$$

This is followed by histogram equalization as:

$$I_{\text{CLAHE}}(x, y) = \left[\frac{\text{CDF}(I(x, y)) - \text{CDF}_{\text{min}}}{\text{CDF}_{\text{max}} - \text{CDF}_{\text{min}}} \times 255 \right]. \quad (7)$$

To preserve the natural appearance of background regions while enhancing diagnostic features, we selectively apply the processing:

$$I_{\text{enhanced}}(x, y) = \begin{cases} I_{\text{CLAHE}}(x, y) & \text{if } \text{Mask}(x, y) = 0, \\ I_{\text{original}}(x, y) & \text{otherwise.} \end{cases} \quad (8)$$

TABLE I
LITERATURE REVIEW SUMMARY OF RECENT STUDIES IN MEDICAL IMAGING.

Reference	Authors	Model / Framework	Task	Dataset(s)	Key findings
Accuracy of SAM in Medical Segmentation [41]	He <i>et al.</i> (2023)	SAM (semantic, point, box prompts)	Medical image segmentation	12 public sets (e.g. BraTS, Kvasir, LiTS)	SAM underperforms in zero-shot medical segmentation; lacks generalization without domain adaptation. ⁷
SAM for Medical Images [42]	Huang <i>et al.</i> (2023)	SAM + medical-tuned prompts	Medical image segmentation	BraTS, ACDC, Prostate, CHAOS	Prompt tuning improves SAM, but still trails task-specific models on medical segmentation.
Experimental Study on SAM for Medical Images [43]	Mazurowski <i>et al.</i> (2023)	SAM (point & box prompts)	Medical image segmentation	19 public sets (e.g. spine MRI, hip X-ray)	IoU: 0.11–0.87
Segment Anything in Medical Images [2]	Ma <i>et al.</i> (2024)	MedSAM (fine-tuned SAM)	Medical image segmentation	1.57 M image–mask pairs across 10 modalities	Outperforms SOTA in 146 tasks
SemiSAM+: Semi-Supervised Segmentation via Foundation Models [13]	Zhang <i>et al.</i> (2025)	SemiSAM+ (SAM + specialist)	Semi-supervised segmentation	Two public sets, one clinical set	Significant improvement with limited annotations
Medical SAM Adapter for Segmentation [18]	Wu <i>et al.</i> (2023)	Medical SAM Adapter (Med-SA)	Medical image segmentation	17 tasks across various modalities	Outperforms SOTA while updating only 2 % of parameters
SAM-Induced Prompt Distillation for Semi-Supervised Segmentation [16]	Huang <i>et al.</i> (2025)	KnowSAM (SAM + LPS + SKD)	Semi-supervised segmentation	Multiple public datasets	Outperforms SOTA in semi-supervised settings
VILA-M3: Expert-Guided VLMs [44]	Nath <i>et al.</i> (2025)	VILA-M3	Multi-task med. VLM	RadQA, MIMIC-CXR, SLAKE, PathVQA, CheXpert, ChestX-ray14	Avg. +9 % over Med-Gemini
VLMs for Report Generation & VQA (Review) [34]	Hartsock <i>et al.</i> (2024)	Various VLMs	Report generation, VQA	MIMIC-CXR, IU-Xray, MedCaT, VQA-RAD, PathVQA, VQA-Med 2020	Performance varies across tasks; challenges in clinical validity and interpretability
Vision Foundation Models in Medical Imaging [35]	Liang <i>et al.</i> (2025)	Various (e.g. SAM, ViT)	Medical image tasks	Multiple public sets	Near-SOTA accuracy with few labels; robustness unresolved
CLIP in Medical Imaging - Survey [45]	Zhao <i>et al.</i> (2025)	CLIP	Various medical tasks	Many public datasets	Contrastive pre-training enables strong zero-shot transfer
Test-Time Adaptation with SaLIP [46]	Aleem <i>et al.</i> (2024)	SaLIP (SAM + CLIP)	Zero-shot segmentation	Brain MRI, Chest X-ray, Fetal US	Dice: 63.46 % (brain), 50.11 % (lung), 30.82 % (fetal head)
UniMed-CLIP for Diverse Modalities [38]	Khattak <i>et al.</i> (2025)	UniMed-CLIP	Multi-modal imaging [38]	UniMed (5.3 M pairs)	+12.61 % over BiomedCLIP
MediCLIP: Few-shot Anomaly Detection [39]	Zhang <i>et al.</i> (2024)	MediCLIP (learnable prompts + adapters)	Few-shot anomaly detection	CheXpert, BrainMRI, BUSI	AUROC: +10 % over SOTA
MedCLIP-SAMv2 for Text-Driven Segmentation [40]	Koleilat <i>et al.</i> (2025)	MedCLIP-SAMv2	Text-driven segmentation	Breast US, Brain MRI, Lung X-ray/CT	Dice: +13.07 % (zero-shot), +11.21 % (weakly supervised)

As shown in Fig. 2, we ensure that contrast enhancement is applied dynamically and adapts to each individual image by leveraging the underlying grayscale intensity distribution, rather than imposing uniform adjustments across the entire dataset. The enhanced output is subsequently validated and converted to an 8-bit representation to ensure numerical stability and compatibility with downstream processing. The pipeline supports parallel batch processing with consistent configuration settings, while allowing key parameters, such as the background intensity threshold, percentile bounds for contrast stretching, CLAHE clip limit [49], and tile grid size, to be tuned for specific datasets. Artifact suppression is achieved through smooth histogram redistribution, bilinear interpolation between tiles, and edge-aware processing strategies. This preprocessing design is particularly well suited for low-contrast medical images, especially CT and MRI scans, where preserving subtle anatomical details is essential for reliable diagnosis and accurate segmentation in subsequent deep learning pipelines.

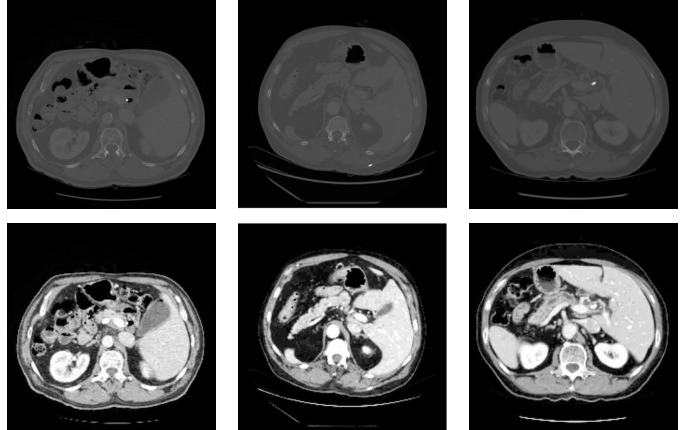


Fig. 2. Representative MRI slices from the FLARE22 dataset [8], showing images before preprocessing (top row) and after preprocessing (bottom row) across three samples.

B. Perturbation-Based XAI

Perturbation-based XAI methods are founded on the principle of systematically modifying input images and observing the corresponding changes in model outputs to infer feature importance. By introducing controlled perturbations to localized regions of an image and measuring their impact on prediction confidence or segmentation outcomes, these approaches identify image regions that contribute most significantly to the model's decision-making process. In this study, we focus on three representative perturbation-based XAI techniques: Local Interpretable Model-agnostic Explanations (LIME) [50], Randomized Input Sampling for Explanation (RISE) [51], and Occlusion Sensitivity analysis [52]. These methods were selected to capture a range of perturbation strategies with complementary strengths and limitations. Importantly, this choice serves as a representative testbed rather than a methodological dependency, as the evaluated XAI techniques are inherently model-agnostic and can be readily applied to alternative segmentation architectures.

1) **LIME**: LIME generates explanations by locally approximating the behavior of a complex model with an interpretable surrogate model [50]. The approach partitions the input image into superpixels and constructs a set of perturbed samples by randomly enabling or disabling these regions [53]. The influence of each superpixel is then estimated by analyzing the corresponding changes in the model's output, enabling identification of regions that most strongly affect the segmentation outcome. In our implementation, we evaluated multiple superpixel generation strategies, including QuickShift, SLIC, and Felzenszwalb, each of which yields distinct explanation heatmaps and emphasizes different spatial and structural characteristics of the segmentation process as shown in Fig 3.

2) **RISE**: RISE generates attribution maps through randomized masking of the input image, wherein multiple masked variants are forwarded through the model and the resulting predictions are aggregated using the corresponding masks as weights [51]. This stochastic sampling process estimates pixel-wise importance by correlating prediction sensitivity with mask presence. In our observations, applying RISE over the entire image space often produced diffuse and less interpretable attribution maps. Consequently, constraining the masking process to organ-specific regions yielded more

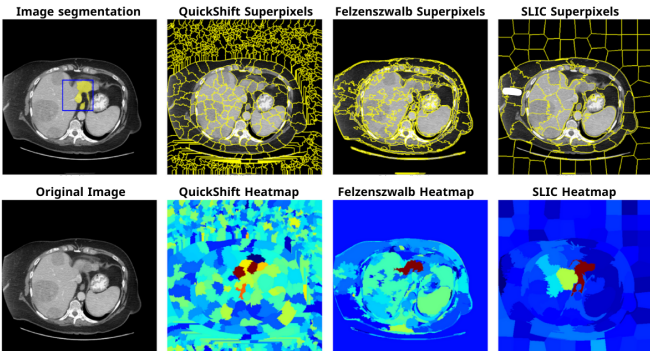


Fig. 3. LIME explanations using different superpixel methods: QuickShift, Felzenszwalb, and SLIC. Top: superpixels; Bottom: Our corresponding heatmaps showing influential regions.

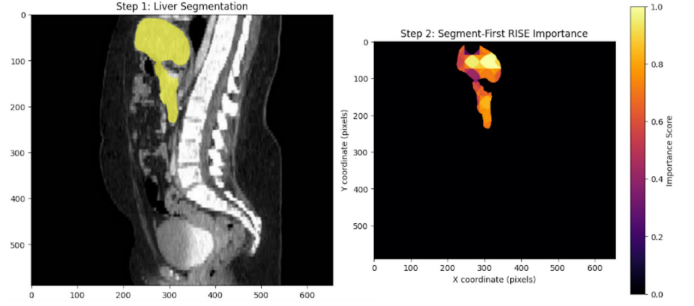


Fig. 4. RISE explanation: input with segmentation (Left) and our corresponding importance map (right) showing contribution of regions to the prediction.

localized and semantically meaningful explanations. Under this region-restricted setting, RISE consistently differentiated between internal organ structures and boundary regions, assigning higher relevance to interior anatomical areas while attenuating spurious activations along edges as shown in Fig 4.

3) **Occlusion Sensitivity Analysis**: Occlusion Sensitivity assesses feature importance by systematically masking localized regions of the input image using a sliding window and measuring the resulting changes in the model's output [54]. By iteratively occluding different spatial locations and quantifying their impact on the segmentation predictions, the method produces an importance map that highlights regions critical to the model's decision process. This straightforward perturbation strategy offers intuitive and easily interpretable explanations and was found to be particularly effective for multi-layer medical imaging data, where the localized occlusion mechanism provides clear insights into the spatial dependencies learned by the segmentation model as shown in Fig 5.

C. Anatomical Region Extraction

We perform region-of-interest (ROI) localization using MediCLIP [39], a medical adaptation of contrastive vision-language pretraining originally proposed for few-shot anomaly detection in medical images [36]. In our framework, MediCLIP is employed as a semantic localization module to guide explainability analysis rather than as a diagnostic classifier. The model is pretrained on medical image-text pairs using the open-clip framework. Input images are preprocessed with aspect ratio preservation to maintain compatibility with the positional embedding grid of the vision-language encoder,

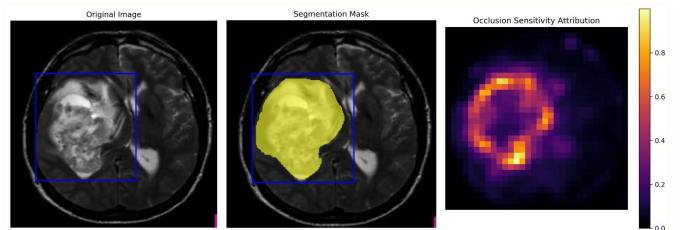


Fig. 5. Occlusion explanation: original input (left), segmentation mask (middle), and our importance heatmap (right) showing regions critical to the prediction.

and corresponding bounding box coordinates are rescaled and shifted to align with the padded image space.

We pass the preprocessed images through the visual encoder to extract token-level embeddings, which are subsequently processed by the Necker module to aggregate multi-scale representations for downstream localization. A learned Adapter further refines these visual features, while a PromptMaker encodes a predefined set of semantic prompts, such as “abnormal organ” or “healthy tissue,” into the shared embedding space. To generate region importance maps, we fuse the adapted visual features with the prompt embeddings using the MapMaker module, producing an output in which a dedicated channel corresponds to abnormal or clinically relevant regions. The resulting importance map is normalized to the range $[0, 1]$, smoothed via Gaussian filtering, and binarized using a fixed threshold (≥ 0.5) to obtain a binary ROI mask. This mask is stored and subsequently used to constrain perturbation-based explainability analyses, ensuring that the generated explanations remain focused on clinically meaningful anatomical regions.

1) CoOp-Based Prompt Optimization: Recent work has increasingly explored the use of context optimization (CoOp) prompt learning as an alternative to manually designed prompts in medical vision-language applications [55]. While handcrafted prompts have proven effective for capturing semantic information in natural images, they often fail to represent the subtle and clinically relevant variations present in medical imagery [39]. To address this limitation, CoOp introduces learnable prompt representations in which each prompt consists of a sequence of trainable word embeddings that are optimized during training. This formulation enables the model to adapt prompt context directly from data, rather than relying on fixed textual descriptions. Importantly, CoOp requires only a limited number of labeled samples to learn effective prompt representations, making it particularly suitable for medical imaging scenarios where annotation is costly and scarce. Formally, the prompt structure is defined as $[V1][V2]...[VM][CLS]$, where $[V]$ denotes learnable context tokens, M is the number of such tokens, and $[CLS]$ represents the class label. These learnable context vectors are concatenated with the class name embeddings to form class-specific prompts, which are subsequently encoded by the vision-language model’s text encoder to produce optimized textual feature representations.

D. Segmentation-guided Organ Localization

To adapt MediCLIP for multi-organ region classification, we reformulate the original anomaly detection formulation into a region-aware semantic learning framework. This transition requires architectural modifications, prompt redefinition, and optimization adjustments to enable explicit spatial reasoning over anatomically meaningful regions rather than generic anomaly localization.

1) From Anomaly Maps to Segmentation Maps: To repurpose the MapMaker module for multi-class organ region classification, we replace the original anomaly map generator with a U-Net architecture [47] that produces dense, per-pixel

predictions. Although the objective is not full organ segmentation, employing a segmentation backbone enables pixel-level classification, which is essential for accurately localizing and distinguishing spatial regions corresponding to different organs. This design allows the model to capture fine-grained spatial structure and contextual relationships between adjacent anatomical regions. In this formulation, input images are first processed by the vision encoder to extract visual embeddings, while predefined textual prompts are encoded using the text encoder. The MapMaker then projects the prompt embeddings to match the dimensionality of the visual features, concatenates the multimodal representations, and employs a U-Net decoder to generate multi-class segmentation maps. This architectural modification effectively shifts the framework from anomaly-centric detection to region-aware semantic classification, making it more suitable for organ-level localization tasks.

2) Prompt-Aware Organ Localization: To support organ-specific regional classification using context optimization, we define a set of semantic classes corresponding to Background and organs. This explicit class formulation aligns the learned representations with anatomical structures of interest and enables the model to produce spatially coherent predictions associated with distinct organ regions. By framing localization as a multi-class semantic prediction problem, the model moves beyond generic anomaly scoring and instead learns structured region-level distinctions that are consistent with anatomical priors.

3) Loss Function Optimization: We optimize the model is performed using a composite loss function that combines multi-class dice loss with categorical cross-entropy. The dice loss extends the conventional binary formulation to the multi-class setting by computing class-wise overlap scores and averaging across all classes, making it particularly effective in medical imaging scenarios characterized by class imbalance and varying organ sizes. Although dice loss is widely used for segmentation tasks [56], it remains well suited for the proposed pixel-wise classification objective, where spatial coherence and regional consistency are critical. The cross-entropy component complements this by enforcing accurate per-pixel classification and penalizing incorrect predictions at a fine-grained level. Together, this combined objective balances region-level overlap accuracy with pixel-level discriminative learning, facilitating stable and anatomically meaningful localization. The combined dice and cross-entropy loss is given as:

$$\mathcal{L}_{\text{total}} = \mathcal{L}_{\text{Dice}} + \mathcal{L}_{\text{CE}}, \quad (9)$$

$$\mathcal{L}_{\text{Dice}} = 1 - \frac{2 \sum_{c=1}^C \sum_{i=1}^N p_i^{(c)} g_i^{(c)}}{\sum_{c=1}^C \sum_{i=1}^N p_i^{(c)} + g_i^{(c)} + \epsilon}, \quad (10)$$

$$\mathcal{L}_{\text{CE}} = - \sum_{i=1}^N \sum_{c=1}^C g_i^{(c)} \log(p_i^{(c)}), \quad (11)$$

where C is the number of classes, N is the number of pixels, $p_i^{(c)}$ is the predicted probability for class c at pixel i , $g_i^{(c)}$ is the ground truth binary label for class c at pixel i , and ϵ is a small constant to avoid division by zero.

E. CLIP-guided Perturbation-based Explainability

The selective application of perturbation-based explainability methods is designed to address a key limitation of such approaches, namely their high computational cost. By restricting perturbations to regions of interest (ROIs) identified through vision-language-guided localization, the explainability process reduces redundant computations while concentrating analysis on clinically meaningful areas. This region-guided strategy significantly decreases the number of patches that must be evaluated, leading to improved runtime efficiency without sacrificing interpretability. For implementation, we employ MedSAM, a medical adaptation of the Segment Anything Model, to generate segmentation masks that serve as the basis for attribution analysis. To ensure seamless integration with perturbation-based explainability frameworks, we introduce a MedSAMWrapper class that encapsulates the model's forward pass and standardizes its interface for compatibility with custom perturbation routines. Selective occlusion sensitivity is then performed by occluding the input image using 64×64 pixel patches with a stride of 32, while explicitly skipping patches that do not intersect with the binary ROI mask. For each retained patch, segmentation is recomputed and the change in Dice score relative to the unperturbed baseline is measured to quantify attribution. These attribution scores are accumulated to form a sensitivity map, which is subsequently normalized for visualization. Overall, this selective perturbation scheme substantially reduces computational overhead and yields more focused, anatomically aligned explanations by confining analysis to clinically relevant regions.

1) Occlusion-based Anatomical Region Extraction: Our anatomical region extraction strategy is built upon a selective occlusion sensitivity framework that concentrates computational effort on clinically relevant anatomical structures. To achieve this, we employ a wrapper-based implementation that preserves the original segmentation model architecture while enabling seamless integration with perturbation-based explainability pipelines. This design ensures compatibility with downstream analysis modules without altering the underlying model behavior, while maintaining spatial consistency and contextual awareness during perturbation.

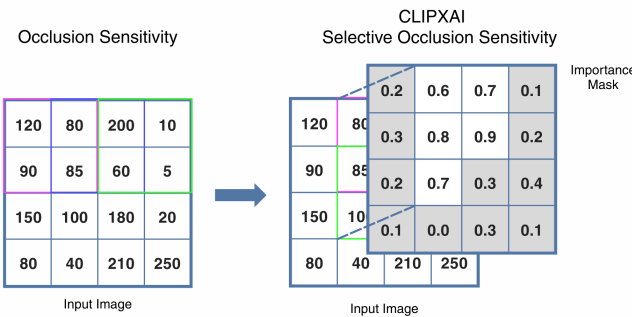


Fig. 6. Comparison of standard occlusion sensitivity (left) and XAI-CLIP-based selective occlusion sensitivity (right). The proposed method incorporates an importance mask to guide occlusion toward informative regions, improving efficiency by avoiding irrelevant areas.

As shown in Fig. 6, the central contribution of this framework is the introduction of ROI-guided importance masking, in which binary or grayscale region-of-interest masks defining anatomically relevant areas are first thresholded to obtain binary representations. These masks are then resized to match the model input resolution using nearest-neighbor interpolation to preserve hard anatomical boundaries and avoid interpolation-induced artifacts. The resulting ROI masks serve as spatial constraints that guide the perturbation process, ensuring that explainability analysis remains focused on meaningful anatomical regions rather than background or irrelevant areas.

Building on this representation, we implement a selective patch processing strategy based on a sliding-window occlusion scheme using 64×64 pixel patches with a stride of 32 pixels. Unlike conventional occlusion sensitivity analysis, patches are processed only if they overlap with the ROI mask, effectively filtering out non-informative regions. This selective mechanism reduces the number of evaluated patches from approximately 10,000 in full-image analysis to between 500 and 2,000 patches, depending on the size of the ROI and the applied importance threshold (e.g., retaining the top 20% most relevant regions). As a result, the proposed strategy achieves a computational reduction of approximately 75-95% while preserving the fidelity of the resulting explanations. The accumulated perturbation responses are aggregated into occlusion heatmaps that highlight anatomically significant regions by quantifying the impact of localized occlusions on segmentation performance, as shown in Fig. 7.

While occlusion sensitivity analysis forms the foundation of the proposed anatomical region extraction methodology, we further investigate complementary perturbation-based explainability techniques, including LIME and RISE, to provide a broader validation of the framework across different attribution mechanisms. This multi-method evaluation enables a more comprehensive assessment of explanation consistency and robustness across diverse perturbation strategies.

2) Analysis of Additional Perturbation Methods: While occlusion sensitivity analysis forms the foundation of our anatomical region extraction methodology, we subsequently explored the RISE approach to provide complementary probabilistic importance estimates. The RISE implementation generates

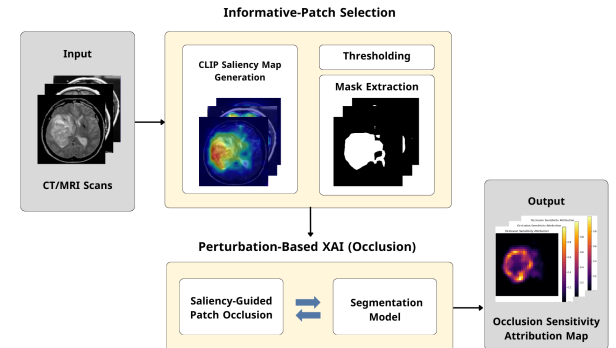


Fig. 7. Overview of the occlusion sensitivity method. Saliency maps are thresholded to extract ROI masks, guiding patch-level occlusion and generating attribution maps for model interpretability.

stochastic binary masks using binomial distribution sampling, producing $N = 2000$ random masks with a configurable density parameter ($p_1 = 0.5$) at a compact 7×7 base resolution. These masks are then upsampled to the full input dimensions using bilinear interpolation. This process reduces the memory footprint by over an order of magnitude compared to full-resolution mask generation (e.g., $\approx 1000 \times$ for a 224×224 image, whereas $214 \times$ would correspond to an $\approx 15 \times 15$ grid) while maintaining adequate spatial precision through upsampling, where optional random shifts of the masks further mitigate grid artifacts.

When applying ROI-constrained perturbation, only pixels within the predefined regions of interest are subjected to perturbation, while pixels outside the ROI are explicitly preserved by assigning a fixed multiplier value of 1.0. This constraint ensures that attribution analysis remains focused on anatomically and clinically relevant areas while preventing spurious effects from background regions. In contrast to the deterministic sliding-window mechanism employed by occlusion sensitivity analysis, RISE adopts a stochastic perturbation strategy based on randomly generated masks, producing probabilistic attribution maps that capture expected importance through aggregation over multiple randomized perturbations.

The methodology further incorporates a dual saliency mapping strategy, in which separate importance maps are generated to capture segmentation fidelity and general ROI relevance, respectively. Independent min-max normalization is applied to each map to preserve relative importance and dynamic range across different anatomical and functional region types, enabling more nuanced interpretation of model behavior across complementary explanatory dimensions.

In further experiments with LIME, we employ Felzenszwalb superpixel segmentation with parameters tailored to medical imaging characteristics. Specifically, the `scale` parameter is set to 100 to balance structural detail preservation with computational efficiency, `sigma` is fixed at 0.5 to apply mild Gaussian smoothing while maintaining organ boundary integrity, and `min_size` is set to 50 to prevent over-fragmentation of non-clinical features. Superpixel generation is constrained to predefined regions of interest by zeroing out pixels outside the ROI and assigning sequential labels to ROI superpixels. This restriction effectively reduces a 512×512 image to approximately 150 semantically meaningful regions, enabling more focused and efficient perturbation analysis.

The perturbation strategy is based on multi-region ablation, in which combinations of superpixels are systematically removed and evaluated, with approximately 200 to 500 perturbation samples generated per image. This formulation enables anatomically grounded explanations by operating on coherent regional groupings rather than isolated pixels, allowing the resulting attributions to align with vascular patterns, organ substructures, and localized pathological regions. To further enhance robustness, a multi-scale analysis is performed by aggregating explanations derived from multiple superpixel scales (50, 100, and 200), thereby capturing features across varying spatial extents, from fine-grained micro-calcifications to larger organ-level structures. Spatial coordinates are preserved throughout the process, ensuring that the resulting

attribution maps remain compatible with downstream clinical workflows and visualization systems.

IV. EXPERIMENTAL SETUP

A. Datasets

For experimental evaluation, we leveraged three publicly available medical imaging datasets. The FLARE22 dataset [8] served as the primary source for training and validation, while additional samples from the SAROS [57] and CHAOS [9] datasets were incorporated for extended testing and validation. All datasets comprise abdominal CT and MRI scans provided in NIfTI format; however, instead of processing full 3D volumes, we extracted 2D axial slices for analysis. Middle axial slices were selected, as they consistently offer clear visualization of key abdominal organs and representative anatomical context. While FLARE22 forms the core experimental dataset, the inclusion of SAROS and CHAOS enables assessment of the robustness and generalizability of the proposed approach across varying imaging protocols and scanner characteristics.

B. Configurations

Experiments were performed on two computational platforms to evaluate performance across heterogeneous hardware configurations. Machine (A) was an Apple M1 Max-based Mac Studio featuring a system-on-chip architecture with a 10-core CPU (8 performance and 2 efficiency cores), a 32-core GPU, and a 16-core Neural Engine, paired with 32 GB of unified LPDDR5-6400 memory (512-bit bus, 400 GB/s bandwidth). This system ran macOS 14 (Sonoma) and utilized PyTorch 2.2 with the Metal backend, operating in BF16 mixed precision. Machine (B) consisted of an NVIDIA RTX 4070 GPU with 12 GB of GDDR6X memory (192-bit bus), an Intel Core i7-13700K processor (16 cores, 24 threads), and 32 GB of DDR5-5600 RAM. This system operated under Windows 11 Pro and employed PyTorch 2.2 with CUDA 12.4 and cuDNN 9, using FP16 mixed precision.

C. Evaluation Metrics

We assess computational efficiency and explanation fidelity using five complementary metrics. Wall-clock latency (T) measures the elapsed time required to process a single 2D slice end to end. Floating-point operations (FLOPs) quantify the computational cost per slice and are computed using $ptflops$ by aggregating the operations incurred during ROI extraction and the N_{patch} MedSAM forward passes executed as part of the perturbation process. Here, N_{patch} denotes the number of occlusion patches actually evaluated and is recorded dynamically within the perturbation loop. The ROI-reduction ratio, defined as $\rho = N_{\text{patch}}/N_{\text{patch}}^{\text{full}}$, captures the fraction of the full patch grid that requires computation, with lower values indicating more effective pruning. Finally, dice coefficient and Intersection-over-Union (IoU) are used to quantify the overlap between the baseline MedSAM segmentation and the segmentation obtained under selective occlusion, serving as fidelity measures to ensure that computational gains do not compromise explanatory reliability.

TABLE II
DICE SCORE AND AUC-ROC PER CLASS

Class	Dice Score	AUC-ROC
Background	0.88	0.86
Liver	0.64	0.97
Right Kidney	0.44	0.97
Left Kidney	0.57	0.99
Spleen	0.24	0.98
Pancreas	0.16	0.97

V. RESULTS AND DISCUSSIONS

A. VLM-based Results

Using the FLARE22 dataset, we conducted experiments with the MediCLIP-based model extended to support multi-class organ region classification. The classification task was defined over five anatomical categories: Background, Liver, Spleen, Right Kidney, and Left Kidney. From the 50 labeled samples provided by FLARE22, we constructed training and validation splits using an 80/20 ratio, with each sample accompanied by corresponding segmentation annotations for the target organs. The model performance was evaluated using class-wise AUC-ROC and dice score. As reported in Table II, the observed dice scores are relatively significant across most classes, which is consistent with the objective of regional anatomical localization rather than precise, pixel-level organ segmentation.

Similarly, as shown in Fig. 9, the model was able to locate five different organs correctly, showing that our approach of combining a U-Net-based segmentation backbone with CoOp prompt learning achieved accurate region-wise classification of organs. This architecture, therefore, is valuable for generating perturbation-based explainability.

B. Perturbation-based Explainability

As shown in Fig. 8, XAI-CLIP consistently delivers substantial computational efficiency gains across all evaluated perturbation-based explainability methods. In particular, the XAI-CLIP-Occlusion variant achieves pronounced runtime reductions of 250 seconds on Machine A and 214 seconds on Machine B, corresponding to efficiency improvements

of 62.3% and 69.4%, respectively. When integrated with LIME, XAI-CLIP further demonstrates significant computational savings, reducing the total cost to 94,431 GFLOPs, which represents a 28.4% reduction relative to the baseline implementation. The RISE-based XAI-CLIP variant similarly exhibits notable efficiency gains, achieving 27-34% reductions in runtime alongside a decrease of 11,078 GFLOPs (6.1%), underscoring the effectiveness of ROI-guided perturbation in reducing computational overhead without compromising explanatory capability.

Similarly, as shown in Table III, using occlusion sensitivity as the underlying perturbation strategy for XAI-CLIP resulted in the most pronounced performance gains among all evaluated methods. Quantitatively, this configuration achieved improvements of 44.6% in Dice coefficient and 96.7% in Intersection-over-Union relative to conventional occlusion-based explanations. These gains are further supported by qualitative assessment, which reveals substantially reduced noise, sharper boundary delineation, and improved spatial coherence in the generated saliency maps when compared to baseline approaches as demonstrated in Fig. 10.

This is worth noting that the LIME-based analysis exhibited notable performance variability, with Dice and IoU values spanning from below 0.1 to as high as 0.893 and 0.802, respectively. In contrast, the traditional LIME baseline frequently failed to localize the target organs altogether, yielding dice scores close to zero in numerous test cases as shown in Fig. 11, highlighting the limitations of unguided perturbation in complex anatomical settings.

Notably, XAI-CLIP-LIME successfully identified anatomical structures even in scenarios where the baseline method completely failed. In instances where both methods achieved reasonable localization, XAI-CLIP-LIME maintained significant heatmap quality, as shown in Fig 12, while simultaneously reducing computational requirements by 28% in GFLOPs and approximately 25% in runtime. However, the consistently poor baseline performance (below 0.1 in many cases) precluded meaningful percentage improvement calculations for this method.

Similarly, RISE-based analysis revealed a counterintuitive yet consistently observed behavior in which regions assigned the lowest importance, corresponding to the darkest areas in the saliency maps, aligned with the true organ locations, while importance progressively increased toward surrounding background tissue as demonstrated in Fig 13. As a result, the generated saliency masks emphasized neighboring structures and background regions rather than the target organs, leading to dice and IoU scores below 0.1 for both the baseline and XAI-CLIP variants due to minimal overlap with ground-truth boundaries. While traditional RISE occasionally produced unstable or image-wide attributions, XAI-CLIP-RISE preserved the same inverted importance trend in a more stable and structured manner, while also achieving a runtime reduction of 287 seconds, corresponding to a 28% improvement.

In summary, we note that while the dice coefficient measures segmentation accuracy through spatial overlap with ground-truth masks, it is inherently sensitive to organ size, which accounts for the lower dice scores observed for smaller

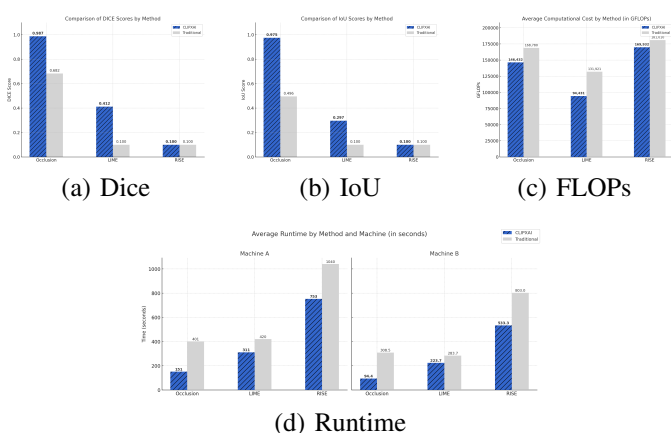


Fig. 8. Quantitative comparison of explainability performance and computational efficiency: (a) Dice score, (b) IoU, (c) FLOPs, and (d) runtime across machines.

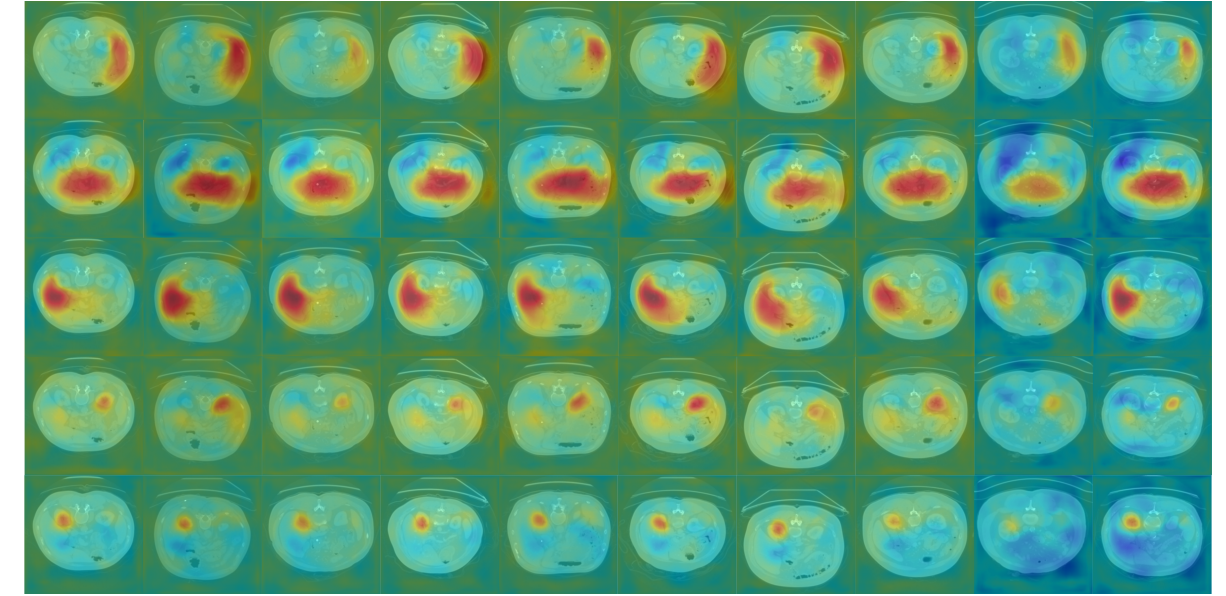


Fig. 9. Results on FLARE22 dataset.

TABLE III

TRADITIONAL VS. XAI-CLIP-GUIDED EXPLAINABILITY. \uparrow INDICATES HIGHER IS BETTER; \downarrow INDICATES LOWER IS BETTER. GRAY ROWS REPORT THE RELATIVE CHANGE OF EACH XAI-CLIP VARIANT COMPARED TO ITS TRADITIONAL COUNTERPART.

Method	Dice \uparrow	IoU \uparrow	GFLOPs \downarrow	Time A \downarrow	Time B \downarrow
Traditional Occlusion	0.6825	0.4956	168,780	401	308.5
XAI-CLIP Occlusion	0.9871	0.9748	146,432	151	94.4
$\Delta_{\text{XAI-CLIP}}$	+44.6%	+96.7%	+13.2%	+62.3%	+69.4%
Traditional LIME	> 0.1	> 0.1	131,921	420	283.7
XAI-CLIP LIME	0.412	0.297	94,431	311	223.7
$\Delta_{\text{XAI-CLIP}}$	—	—	+28.4%	+26.0%	+21.1%
Traditional RISE	> 0.1	> 0.1	181,010	1,040	533.3
XAI-CLIP RISE	> 0.1	> 0.1	169,932	753	803
$\Delta_{\text{XAI-CLIP}}$	—	—	+6.1%	+27.6%	+33.6%

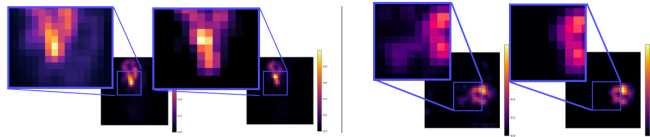


Fig. 10. Occlusion-sensitivity heat-map of the model output.

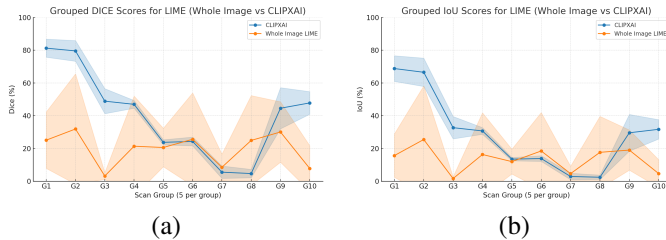


Fig. 11. (a) Distribution of Dice values for Traditional LIME vs. XAI-CLIP. (b) Distribution of IoU values for Traditional LIME vs. XAI-CLIP.

structures such as the spleen and pancreas. In contrast, AUC-ROC evaluates the model’s ability to assign higher confidence to true organ pixels relative to background without thresholding probabilistic outputs, making it particularly informative for assessing region-level confidence even when boundary delineation is imperfect. The computational efficiency gains achieved by the proposed framework arise directly from restricting perturbations to anatomically relevant regions, thereby avoiding unnecessary evaluations over background areas. Notably, the observed behavior in RISE-based explanations suggests that the segmentation model leverages contextual and boundary information surrounding organs more heavily than intra-organ texture cues; consequently, masking interior regions has limited impact on predictions, leading to low attributed importance for clinically relevant interiors despite their diagnostic significance.

VI. CONCLUSIONS

Explainable artificial intelligence remains a fundamental requirement for the safe and trustworthy deployment of med-

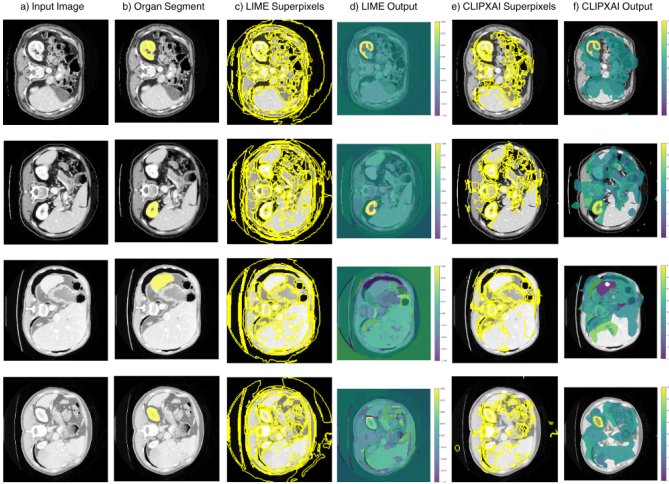


Fig. 12. LIME visualizations across different processing stages (a–f).

ical image segmentation systems in clinical practice. In this work, we presented XAI-CLIP, a region-guided explainability framework that integrates vision-language representations, prompt-based learning, and segmentation models to enhance perturbation-based explanations. By leveraging semantically informed region localization, the proposed approach produces clearer, anatomically meaningful attribution maps while significantly reducing the computational cost associated with conventional perturbation strategies. Experimental results demonstrate that XAI-CLIP improves both interpretability and efficiency across multiple explainability methods and datasets. Future work will explore further optimization of the framework and its validation on large-scale, real-world clinical datasets to support robust and clinically deployable explainable medical imaging systems.

REFERENCES

[1] J. De Fauw, J. R. Ledsam, B. Romera-Paredes, S. Nikolov, N. Tomasev, S. Blackwell, H. Askham, X. Glorot, B. O’Donoghue, D. Visentin, *et al.*, “Clinically applicable deep learning for diagnosis and referral in retinal disease,” *Nature Medicine*, vol. 24, no. 9, pp. 1342–1350, 2018.

[2] J. Ma, Y. He, F. Li, L. Han, C. You, and B. Wang, “Segment anything in medical images,” *arXiv preprint arXiv:2304.12306*, vol. v3, Apr 2024.

[3] T. Rädsch, A. Reinke, V. Weru, M. D. Tizabi, N. Schreck, A. E. Kavur, B. Pekdemir, T. Roß, A. Kopp-Schneider, and L. Maier-Hein, “Labelling instructions matter in biomedical image analysis,” *Nature Machine Intelligence*, vol. 5, no. 3, pp. 273–283, 2023.

[4] S. Lapuschkin, S. Wäldchen, A. Binder, G. Montavon, W. Samek, and K.-R. Müller, “Unmasking clever hans predictors and assessing what machines really learn,” *Nature Communications*, vol. 10, no. 1, p. 1096, 2019.

[5] A. Chattopadhyay, A. Sarkar, P. Howlader, and V. N. Balasubramanian, “Grad-cam++: Generalized gradient-based visual explanations for deep convolutional networks,” *CoRR*, vol. abs/1710.11063, 2017.

[6] T. Abe and Y. Asai, “Towards a perturbation-based explanation for medical ai as differentiable programs,” *arXiv preprint arXiv:2502.14001*, 2025.

[7] A. Kirillov, E. Mintun, N. Ravi, H. Mao, C. Rolland, L. Gustafson, T. Xiao, S. Whitehead, A. C. Berg, W.-Y. Lo, P. Dollár, and R. Girshick, “Segment anything,” *arXiv preprint arXiv:2304.02643*, 2023.

[8] J. Ma, Y. Zhang, S. Gu, C. Ge, S. Ma, A. Young, C. Zhu, K. Meng, X. Yang, Z. Huang, F. Zhang, W. Liu, Y. Pan, S. Huang, J. Wang, M. Sun, W. Xu, D. Jia, J. W. Choi, N. Alves, B. de Wilde, G. Koehler, Y. Wu, M. Wiesenfarth, Q. Zhu, G. Dong, J. He, F. C. Consortium, and B. Wang, “Unleashing the strengths of unlabeled data in pan-cancer abdominal organ quantification: the flare22 challenge,” *arXiv preprint arXiv:2308.05862*, 2023.

[9] A. E. Kavur, N. S. Gezer, M. Bariş, S. Aslan, P.-H. Conze, V. Groza, D. D. Pham, S. Chatterjee, P. Ernst, S. Özkan, B. Baydar, D. Lachinov, S. Han, J. Pauli, F. Isensee, M. Perkonigg, R. Sathish, R. Rajan, D. Sheet, G. Dovletov, O. Speck, A. Nürnberg, K. H. Maier-Hein, G. B. Akar, G. Ünal, O. Dicle, and M. A. Selver, “Chaos challenge—combined (ct-mr) healthy abdominal organ segmentation,” *Medical Image Analysis*, vol. 69, p. 101950, 2021.

[10] S. He, R. Bao, J. Li, J. Stout, A. Bjornerud, P. E. Grant, and Y. Ou, “Accuracy of segment-anything model (sam) in medical image segmentation tasks,” *arXiv preprint arXiv:2304.09324*, 2023.

[11] Y. Huang, X. Yang, L. Liu, and D. Ni, “Segment anything model for medical images?,” *Medical Image Analysis*, vol. 89, p. 102918, 2023.

[12] M. A. Mazurowski, H. Dong, H. Gu, J. Yang, N. Konz, and Y. Zhang, “Segment anything model for medical image analysis: an experimental study,” *Medical Image Analysis*, vol. 89, p. 102918, 2023.

[13] Y. Zhang, B. Lv, L. Xue, W. Zhang, Y. Liu, Y. Fu, Y. Cheng, and Y. Qi, “Semisam+: Rethinking semi-supervised medical image segmentation in the era of foundation models,” *arXiv preprint arXiv:2502.20749*, 2025.

[14] J. Wu, Y. Wang, W. Zhang, Y. Zhang, and Y. Qi, “Medical sam adapter: Adapting segment anything model for medical image segmentation,” *arXiv preprint arXiv:2306.01250*, 2023.

[15] J. Ruan, Y. Zhang, Y. Wang, and Y. Qi, “Vm-unet: Vision mamba unet for medical image segmentation,” *arXiv preprint arXiv:2402.02491*, 2024.

[16] K. Huang, Y. Li, Y. Wang, Y. Zhang, and Y. Qi, “Learnable prompting sam-induced knowledge distillation for semi-supervised medical image segmentation,” *IEEE Transactions on Medical Imaging*, vol. 44, no. 5, pp. 2295–2306, 2025.

[17] J. Wu, Y. Fu, Y. Zhang, and Y. Qi, “Medical sam adapter: Adapting segment anything model for medical image segmentation,” *arXiv preprint arXiv:2304.12620*, 2025.

[18] R. Wu, Y. Liu, P. Liang, and Q. Chang, “Ultralight vm-unet: Parallel vision mamba significantly reduces parameters for skin lesion segmentation,” *arXiv preprint arXiv:2403.20035*, 2024.

[19] M. Fontes, J. P. C. de Almeida, and A. M. D. Cunha, “Application of example-based explainable artificial intelligence (xai) for analysis and

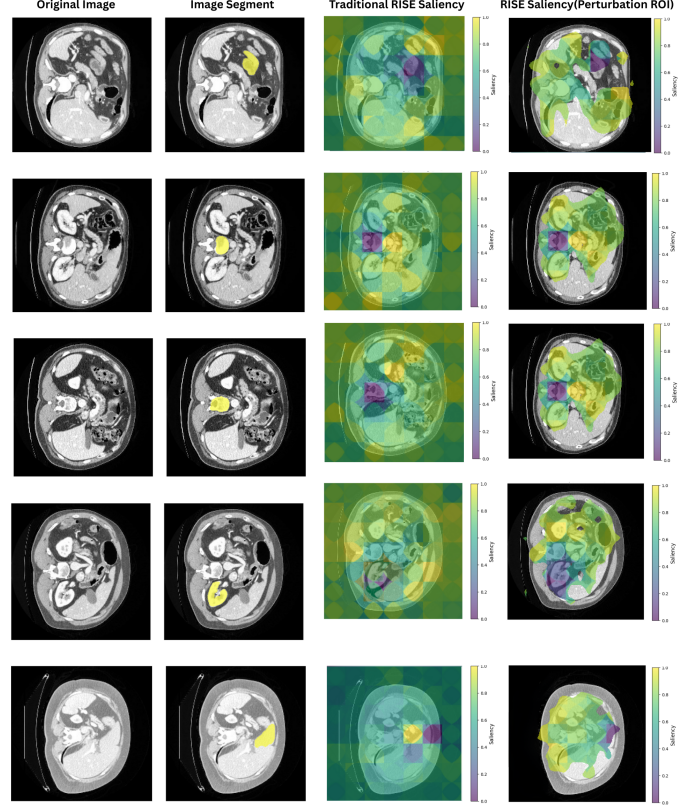


Fig. 13. RISE visualizations across different processing stages (a–d).

interpretation of medical imaging: A systematic review," *IEEE Access*, vol. 12, pp. 26419–26427, 2024.

[20] J. Hou, S. Liu, Y. Bie, H. Wang, A. Tan, L. Luo, and H. Chen, "Self-explainable ai for medical image analysis: A survey and new outlooks," *arXiv preprint arXiv:2410.02331*, 2024.

[21] G. Iglesias, H. Menendez, and E. Talavera, "Improving explanations for medical x-ray diagnosis combining variational autoencoders and adversarial machine learning," *Computers in Biology and Medicine*, vol. 188, p. 109857, 2025.

[22] T. Abe and Y. Asai, "Towards a perturbation-based explanation for medical ai as differentiable programs," *arXiv preprint arXiv:2502.14001*, 2025.

[23] Q. Mastoi, S. Latif, S. Brohi, J. Ahmad, A. Alqhatani, A. Alshehri, A. Al Mazroa, and R. Ullah, "An interpretable and collaborative federated learning model for brain tumor classification using mri images," *Frontiers in Oncology*, vol. 15, p. 11903279, 2025.

[24] T. Yoshida, H. Nakamura, Y. Sato, E. Tanaka, and K. Suzuki, "Explainable artificial intelligence-assisted exploration of clinically relevant biomarkers in optical coherence tomography," *Ophthalmology Science*, vol. 5, p. 100102, 2025.

[25] C. Qiu, Y. Wu, W. Ke, X. Bai, and T. Zhang, "Refining clip's spatial awareness: A visual-centric perspective," in *International Conference on Learning Representations (ICLR)*, 2025. Poster.

[26] A. Radford, J. W. Kim, C. Hallacy, A. Ramesh, G. Goh, S. Agarwal, G. Sastry, A. Askell, P. Mishkin, J. Clark, G. Krueger, and I. Sutskever, "Learning transferable visual models from natural language supervision," in *Proceedings of the 38th International Conference on Machine Learning*, 2021.

[27] P. Poudel, Y. Liu, Y. Li, and Y. Qi, "Transferability of vision-language segmentation models to 2d medical image segmentation," *arXiv preprint arXiv:2405.00954*, 2024.

[28] A. Dhakal, Y. Zhang, Y. Wang, Y. Li, and Y. Qi, "Vlsm-adapter: Parameter-efficient fine-tuning for medical vision-language segmentation," *arXiv preprint arXiv:2405.06196*, 2024.

[29] J. Dietlmeier, S. Aleem, K. Curran, N. E. O'Connor, and S. Little, "Vlsm-ensemble: Combining vision-language segmentation models with lightweight unet variants," *arXiv preprint arXiv:2504.02153*, 2025.

[30] W. Chen, X. Zhang, Z. Wang, and L. Xu, "Causalclipseg: Referring medical image segmentation via causal inference and cross-modal alignment," in *MICCAI 2025*, 2025.

[31] A. Sultan, Y. Li, and Y. Qi, "Bipvl-seg: Bidirectional progressive vision-language fusion for medical image segmentation," *arXiv preprint arXiv:2503.23534*, 2025.

[32] W. Chen, Y. Li, Y. Wang, and Y. Qi, "Bi-vlqm: Bi-level class-severity-aware vision-language graph matching for text-guided medical image segmentation," *arXiv preprint arXiv:2410.12345*, 2025.

[33] A. Nath, Y. Du, Y. Xue, H. Wang, and X. Wang, "Vila-m3: Expert-guided instruction fine-tuning for medical vision-language models," *arXiv preprint arXiv:2504.07825*, 2025.

[34] J. Hartsock and G. Rasool, "A survey of vision-language models for medical report generation and visual question answering," *Frontiers in Artificial Intelligence*, vol. 7, 2024.

[35] P. Liang, H. Chen, Y. Liu, Y. Xie, and G. Wang, "Adapting vision foundation models for medical image segmentation: A comprehensive review," *arXiv preprint arXiv:2502.14584*, 2025.

[36] Z. Zhao, Y. Liu, H. Wu, M. Wang, Y. Li, S. Wang, L. Teng, D. Liu, Z. Cui, Q. Wang, and D. Shen, "Clip in medical imaging: A comprehensive survey," *Medical Image Analysis*, vol. 92, p. 103551, 2025.

[37] S. Aleem, F. Wang, M. Maniparambil, E. Arazo, J. Dietlmeier, K. Curran, N. E. O'Connor, and S. Little, "Test-time adaptation with salip: A cascade of sam and clip for zero-shot medical image segmentation," in *Proceedings of the IEEE/CVF Conference on Computer Vision and Pattern Recognition Workshops (CVPRW)*, pp. 5184–5193, 2024.

[38] M. U. Khattak, S. K. Kunhimon, M. Naseer, S. Khan, and F. S. Khan, "Unimed-clip: Towards a unified image-text pretraining paradigm for diverse medical imaging modalities," *arXiv preprint arXiv:2412.10372*, 2024.

[39] X. Zhang, M. Xu, D. Qiu, R. Yan, N. Lang, and X. Zhou, "Mediclip: Adapting clip for few-shot medical image anomaly detection," in *Medical Image Computing and Computer Assisted Intervention – MICCAI 2024*, Lecture Notes in Computer Science, Springer, 2024.

[40] T. Koleilat, H. Asgariandehkordi, H. Rivaz, and Y. Xiao, "Medclip-samv2: Towards universal text-driven medical image segmentation," *arXiv preprint arXiv:2409.19483*, 2025.

[41] S. He, R. Bao, J. Li, J. Stout, A. Bjørnerud, P. E. Grant, and Y. Ou, "Computer-vision benchmark segment-anything model (sam) in medical images: Accuracy in 12 datasets," *arXiv preprint*, 2025.

[42] Y. Huang, X. Yang, L. Liu, H. Zhou, A. Chang, X. Zhou, R. Chen, J. Yu, J. Chen, C. Chen, S. Liu, H. Chi, X. Hu, K. Yue, L. Li, V. Grau, D.-P. Fan, F. Dong, and D. Ni, "Segment anything model for medical images?," *Medical Image Analysis*, vol. 92, p. 103061, Feb. 2024.

[43] M. A. Mazurowski, H. Dong, H. Gu, J. Yang, N. Konz, and Y. Zhang, "Segment anything model for medical image analysis: An experimental study," *Medical Image Analysis*, vol. 89, p. 102918, Oct. 2023.

[44] V. Nath, W. Li, D. Yang, A. Myronenko, M. Zheng, Y. Lu, Z. Liu, H. Yin, Y. Tang, P. Guo, C. Zhao, Z. Xu, Y. He, G. Heinrich, Y. M. Law, B. Simon, S. Harmon, S. Aylward, M. Edgar, M. Zephyr, S. Han, P. Molchanov, B. Turkbey, H. Roth, and D. Xu, "Vila-m3: Enhancing vision-language models with medical expert knowledge," 2025.

[45] Z. Zhao, Y. Liu, H. Wu, M. Wang, Y. Li, S. Wang, L. Teng, D. Liu, Z. Cui, Q. Wang, and D. Shen, "Clip in medical imaging: A survey," *Medical Image Analysis*, vol. 102, p. 103551, May 2025.

[46] S. Aleem, F. Wang, M. Maniparambil, E. Arazo, J. Dietlmeier, G. Silvestre, K. Curran, N. E. O'Connor, and S. Little, "Test-time adaptation with salip: A cascade of sam and clip for zero shot medical image segmentation," 2024.

[47] O. Ronneberger, P. Fischer, and T. Brox, "U-net: Convolutional networks for biomedical image segmentation," in *International Conference on Medical Image Computing and Computer-Assisted Intervention (MICCAI)*, pp. 234–241, Springer, 2015.

[48] A. Mishra, "Contrast limited adaptive histogram equalization (clahe) approach for enhancement of the microstructures of friction stir welded joints," *Advances in Mechanics*, vol. 9, no. 3, pp. 216–240, 2021.

[49] V. Stimper, S. Bauer, R. Ernststorfer, B. Schölkopf, and R. P. Xian, "Multidimensional contrast limited adaptive histogram equalization," *IEEE Access*, vol. 7, pp. 165437–165447, 2019.

[50] B. Aldughayiq, F. Ashfaq, N. Jhanjhi, and M. Humayun, "Explainable ai for retinoblastoma diagnosis: Interpreting deep learning models with lime and shap," *Diagnostics*, vol. 13, no. 11, p. 1932, 2023.

[51] J. Highton, Q. Z. Chong, R. Crawley, J. A. Schnabel, and K. K. Bhatia, "Evaluation of randomized input sampling for explanation (rise) for 3d xai – proof of concept for black-box brain-hemorrhage classification," in *International Conference on Medical Imaging and Computer-Aided Diagnosis (MICAD)*, vol. 1166 of *Lecture Notes in Electrical Engineering*, pp. 41–51, Springer, 2024.

[52] Z. Gandomkar, P. L. Khong, A. Punch, and S. Lewis, "Using occlusion-based saliency maps to explain an artificial intelligence tool in lung cancer screening: Agreement between radiologists, labels, and visual prompts," *Journal of Digital Imaging*, vol. 35, no. 5, pp. 1164–1175, 2022.

[53] D. Bhati, F. Neha, and M. Amiruzzaman, "A survey on explainable artificial intelligence (xai) techniques for visualizing deep learning models in medical imaging," *Journal of Imaging*, vol. 10, no. 10, p. 239, 2024.

[54] M. Resta, A. Monreale, and D. Bacciu, "Occlusion-based explanations in deep recurrent models for biomedical signals," *Entropy*, vol. 23, no. 8, p. 1064, 2021.

[55] T. Koleilat, H. Asgariandehkordi, H. Rivaz, and Y. Xiao, "Biomedcoop: Learning to prompt for biomedical vision-language models," *arXiv preprint arXiv:2411.15232*, 2024.

[56] J. Bertels *et al.*, "Optimizing the dice score and jaccard index for medical image segmentation: Theory and practice," in *Medical Image Computing and Computer-Assisted Intervention – MICCAI 2019*, pp. 92–100, Springer, 2019.

[57] A. R. Nori, Z. Lu, A. Prakash, K. Somasundaram, D. Bar, *et al.*, "Saros: A semi-supervised annotated radiology report open-source corpus for clinical research," *npj Digital Medicine*, vol. 6, no. 1, pp. 1–10, 2023.